

1 **Phytoplankton dynamics driven by vertical nutrient fluxes during the spring**
2 **inter-monsoon period in the northeastern South China Sea**

3

4 Qian P. Li*, Yuan Dong, Yanjun Wang

5 South China Sea Institute of Oceanology, Chinese Academy of Sciences, Guangzhou,
6 China

7

8

9 Submitted to Biogeosciences on March 27, 2015

10 Revised July 29, 2015

11 2nd revised October 5, 2015

12 3nd revised November 30, 2015

13 Accepted, December 24, 2015

14

15 *Correspondence to: qianli@scsio.ac.cn

16 **Abstract**

17 A field survey from the coastal ocean zones to the offshore pelagic zones of the
18 northeastern South China Sea (nSCS) was conducted during the inter-monsoon period of
19 May 2014 when the region was characterized by prevailing low-nutrient conditions.
20 Comprehensive field measurements were made for not only hydrographic and
21 biogeochemical properties but also phytoplankton growth and microzooplankton grazing
22 rates. We also performed estimations of the vertical turbulent diffusivity and diffusive
23 nutrient fluxes using a Thorpe-scale method and the upwelling nutrient fluxes by Ekman
24 pumping using satellite-derived wind stress curl. Our results indicated a positive
25 correlation between the integrated phytoplankton chlorophyll-*a* and vertical nutrient
26 fluxes in the offshore region of the nSCS during the study period. We generally found an
27 increasing role of turbulent diffusion but a decreasing role of curl-driven upwelling in
28 vertical transport of nutrients from the coastal ocean zones to the offshore pelagic zones.
29 Elevated nutrient fluxes near Dongsha Islands supported high new production leading to
30 net growth of the phytoplankton community, whereas the low fluxes near southwest
31 Taiwan had resulted in a negative net community growth leading to decline of a surface
32 phytoplankton bloom. Overall, phytoplankton dynamics in the large part of the nSCS
33 could be largely driven by vertical nutrient fluxes including turbulent diffusion and
34 curl-driven upwelling during the spring inter-monsoon period.

35

36

37 **1. Introduction**

38 Nutrient fluxes from below the euphotic zone are essential for phytoplankton primary
39 production in the surface ocean (Eppley and Peterson, 1979), while the mechanisms
40 regulating those fluxes are still inadequately understood in the northeastern South China
41 Sea (nSCS), particularly during the spring intermonsoon period. Wind-driven coastal
42 upwelling, river discharge, and inter-shelf nutrient transport were important mechanisms
43 supplying nutrients to the euphotic zone of the nSCS (Liu et al., 2002; Gan et al., 2010;
44 Han et al., 2013), while their contributions to primary production were mostly limited to
45 coastal regions as these nutrients would be mostly utilized in the coastal waters before
46 reaching the large area of the nSCS. Kuroshio intrusion would dilute the nSCS waters
47 with the low nutrient North Pacific waters (Farris and Wimbush, 1996), which appeared
48 to be much weaker during April-September (Centurioni et al., 2004). Contribution of
49 nitrogen fixation to new production of the nSCS was generally negligible compared to the
50 nitrate-based new production (Chen et al., 2005; Bombar et al., 2010). Atmospheric
51 deposition of anthropogenic nitrogen could support up to ~20% of the annual new
52 production in the nSCS exceeding those from riverine inputs (Kim et al., 2014). However,
53 its contribution would be much less during the spring inter-monsoon season as the
54 reduced rate of atmospheric deposition (Lin et al., 2009).

55 Diapycnal mixing by turbulent dissipation was recently found to be important for the
56 supply of new nitrogen in the nSCS, where the vertical turbulent diffusivities were an
57 order of magnitude higher than the adjacent West Pacific Ocean (Tian et al., 2009; Liu
58 and Lozovatsky, 2012; Yang et al., 2014). It was also suggested that phytoplankton
59 blooms off the west coast of the nSCS could be induced by wind stress curl-driven
60 upwelling during the spring inter-monsoon season (Wang and Tang, 2014), which would
61 cause a local uplift of isopycnals leading to nutrient injection into the euphotic zone with
62 subsequent changes of community structure and productivity (Rykaczewski and Checkley,
63 2008; Li et al., 2015). By modifying the surface wind stress and wind stress curl via
64 air-sea coupling, the eddy-induced Ekman pumping (Gaube et al., 2013) was important
65 for phytoplankton production in the nSCS during the inter-monsoon transition period (Lin
66 et al., 2010). As both intermittent turbulent diffusion and wind-driven Ekman pumping
67 affect the vertical transport of nutrients on temporal scales similar to the generation time

68 of phytoplankton, they will have large influences on plankton dynamics of the upper
69 ocean (Cullen et al., 2002). It is therefore important to investigate the roles of these two
70 mechanisms in driving the variability of phytoplankton biomass and primary production
71 in the large area of the nSCS.

72 Spatial distribution of phytoplankton at sea is a result of complex interactions
73 between physical and biological processes (Davis et al., 1991; Abraham, 1998). In
74 addition to the vertical nutrient fluxes, phytoplankton biomass and productivity of the
75 nSCS are influenced by growth-grazing dynamics (Chen, 2005; Huang et al., 2011; Zhou
76 et al., 2011; Chen et al., 2013). Shifts in the dominance of phytoplankton species in the
77 western South China Sea were believed to be driven by a close coupling of the mortality
78 rates of different phytoplankton groups via common grazers such as nanoflagellates
79 (Chen et al., 2009). There was on average ~61% of phytoplankton growth lost to
80 microzooplankton grazing in coastal upwelling regions of the nSCS in response to
81 increased nutrient fluxes, whereas growth and grazing mortality rates were mostly
82 balanced on the shelf and shelf break areas without upwelling events (Huang et al., 2011).
83 It was also suggested that the balance of phytoplankton growth and microzooplankton
84 grazing in the pelagic nSCS could be perturbed by physical disturbances such as eddies,
85 fronts, and typhoons, leading to large deviations of planktonic ecosystem from the steady
86 state (Zhou et al., 2011; Chen et al., 2013).

87 Here, we present results of a field survey from the coastal ocean zones to the offshore
88 pelagic zones in the nSCS conducted during the spring inter-monsoon transition of May
89 2014, when the region was characterized by prevailing low nutrient conditions as a result
90 of weak and variable winds (Lin et al., 2010). Comprehensive measurements were made
91 for hydrographic and biogeochemical properties, as well as biological rates including
92 phytoplankton growth and grazing rates and net nutrient consumption rates. We also
93 performed estimations of the vertical turbulent diffusivity and diffusive nutrient fluxes
94 using a Thorpe-scale method (Gargett and Garner, 2008; Li et al., 2012) and the
95 upwelling nutrient fluxes by Ekman pumping using satellite-derived wind stress curl (Gill,
96 1982; Risien and Chelton, 2008). In synthesizing these field data, the focus of this paper
97 are to (1) investigate the spatial patterns of vertical nutrient fluxes in the nSCS, (2)
98 determine the relative roles of turbulent diffusion and Ekman pumping to vertical

99 transport of nutrients in the upper ocean, and (3) understand the linkage between vertical
100 nutrient fluxes and phytoplankton dynamics in the nSCS during the spring inter-monsoon
101 period.

102

103 **2. Materials and methods**

104 **2.1. Site description, field sampling, and measurements**

105 There are typically high nutrients in the coastal regions of the nSCS due to river
106 discharge, inter-shelf transport, and upwelling and mixing (Gan et al., 2010), in contrast
107 to the oligotrophic low-latitude offshore regions with strong stratification. The nSCS is
108 also strongly influenced by Kuroshio intrusion through the Luzon Strait (Farris and
109 Wimbush, 1996). The intruded Kuroshio waters with higher temperature and salinity but
110 lower nutrients are often transported westward via eddies and Ekman advection
111 (Centurioni et al., 2004) influencing the large area of the nSCS on seasonal time-scales.

112 A field survey of the nSCS (Fig. 1) was conducted during May 2014 aboard the *R/V*
113 *Shiyan III* of the South China Sea Institute of Oceanology. From May 14th to May 16th,
114 2014, a transect from the coastal waters near Shantou to the offshore waters near the
115 Luzon Strait was comprehensively sampled to investigate the spatial patterns of
116 hydrographic and biogeochemical properties of the nSCS. Station S₁ (22°N, 119.5°E) was
117 chosen as a reference time-series station with continuous CTD sampling of 13 casts
118 within 24 hours (start: 10:00 am, May 18th, 2014). Stations A (21.9°N, 120°E with a
119 bottom depth of 1547 m) near the southwest of Taiwan and station B (20.5°N, 117°E with
120 a bottom depth of 607 m) in the southeast of Dongsha Islands were selected for dilution
121 experiments to quantify phytoplankton growth and microzooplankton grazing rates.

122 Discrete seawater samples at depths of 0 m, 25 m, 50 m, 75 m, 100 m, 200 m, 300 m,
123 500 m, and 700 m were collected using a SeaBird SBE 9/11 CTD rosette water sampler
124 system, providing high resolution hydrographic measurements of the upper water column
125 with internal pressure, conductivity, and temperature sensors. We define euphotic zone as
126 the layer above 1% of surface Photosynthetically Active Radiation (PAR), measured by a
127 PAR sensor (QSP200L, Biospherical Instrument, Inc.). After inline filtrations from the
128 PVC Niskin bottles through 0.8 μm Nuclepore filters, seawater samples for nutrients
129 were frozen immediately and stored in a refrigerator until final analyses after the cruise.

130 For chlorophyll-*a* sampling, 500 ml of seawater was gently filtered (<50 mmHg) through
131 a GF/F (Whatman) filter, which was wrapped in a piece of aluminum foil and kept at
132 -20°C on board. Upon return to the lab, chlorophyll-*a* samples were sonicated for 20 min
133 and extracted in 5 ml 90% acetone at 4°C in the dark for 24 hours. These samples were
134 centrifuged at 4000 rpm for 10 min before final determinations by standard fluorescence
135 methods (Parsons et al., 1984) using a Turner Designs Model 10 Fluorometer.
136 Concentrations of nitrate plus nitrite, phosphate and silicate were determined by a Seal
137 AA3 auto analyzer (Bran-Luebbe, GmbH). The low concentrations of nitrate plus nitrite
138 and phosphate within the euphotic zone were also determined by the long-cell method (Li
139 et al., 2008; Li and Hansell, 2008) by incorporating a 50 cm liquid waveguide cell to AA3
140 with detection limits of ~0.02 µM and ~0.01 µM, respectively.

141

142 2.2. Remote sensing observations

143 High-resolution satellite data, including sea surface temperature (SST), sea surface
144 chlorophyll (SSChl), surface geostrophic velocities, as well as surface wind stresses and
145 Ekman velocities, were used to assess the spatial change of these surface properties in the
146 nSCS during the study period. Monthly averaged sea surface chlorophyll-*a* (0.04°×0.04°)
147 was acquired from the NASA's Moderate Resolution Imaging Spectroradiometer data
148 observed by the Aqua Satellite (MODIS-Aqua). Surface velocity fields (0.3°×0.3°) were
149 derived from multi-satellite altimeter (TOPEX, JASON-1, ERS-2, ENVISAT and GFO)
150 and scatterometer data distributed by the NOAA's Ocean Surface Current Analysis
151 -Realtime (OSCAR) program, which had been largely validated by a variety of field
152 measurements including global drifts, moorings, and shipboard ADCP. Daily sea surface
153 temperature (0.1°×0.1°) was acquired from the NOAA's Geostationary Operational
154 Environmental Satellite –Polar Operational Environmental Satellite program
155 (GOES-POES). Daily Ekman upwelling velocities and surface wind stresses with a
156 resolution of 0.25°×0.25° were derived from the Advanced Scatterometer data by the
157 European Meteorological and Operational satellite program (METOP-ASCAT). The
158 Ekman pumping velocity (w_e , negative for downwelling) at the depth of Ekman layer is
159 calculated as (Gill, 1982)

160

$$w_e = \frac{1}{\rho_w} \left(\nabla \times \frac{\tau}{f} \right)$$

161 (1)

162 where ρ_w is the density of seawater, which is assumed constant at 1024 kg m^{-3} ; f is the
163 Coriolis parameter; τ is the vector of wind stress.

164

165 2.3 Thorpe-scale analyses and vertical diffusivity

166 We applied a Thorpe-scale based approach (Thorpe, 1977; Galbraith and Kelley, 1996;
167 Gargett and Garner, 2008; Li et al., 2012) to estimate fine structure and turbulent
168 diffusivity for each station using CTD downcast data. The method combines several
169 criteria to determine the real overturns from a density profile (Li et al., 2012), including
170 the test of minimum thickness, the run-length and water mass tests (Galbraith and Kelley
171 1996), as well as the tests of minimal overturn ratio and maximal T/S tightness (Gargett
172 and Garner, 2008). These criteria ensure that the maximal density difference within an
173 overturn is greater than twice the measurement noise (0.001 kg m^{-3}). The length scale of
174 an overturn is larger than twice the vertical resolution (Nyquist theorem) and larger than a
175 minimum thickness (Galbraith and Kelley, 1996). The percentage of positive/negative
176 displacements within an overturn (the overturn ratio) is larger than 0.2 and the deviations
177 on a T/S diagram are less than 0.003 (Gargett and Garner, 2008). The vertical resolution
178 of CTD sampling during the cruise was $\sim 10 \text{ cm}$ with a fall rate of $\sim 2.4 \text{ m s}^{-1}$. Therefore,
179 only overturns larger than 0.5 m are included, to obtain five data point resolution. We
180 discard data in the upper 10 m, as the Thorpe approach is not strictly valid there. Once an
181 overturn is identified, the Thorpe scale (L_T) is calculated from the root mean square of the
182 vertical displacement (d_z) as $L_T = (\sum d_z^2)^{0.5}$.

183 Turbulent kinetic energy dissipation rate (ε) is calculated from L_T and N by

184

$$\varepsilon = 0.64 \cdot L_T^2 \cdot N^3$$

185 (2)

186 where N is the buoyancy frequency given by $N^2 = -g\rho_0^{-1}(\partial\rho/\partial z)$ with g the gravitational
187 acceleration, ρ_0 the mean density, and $\partial\rho/\partial z$ the density gradient across each overturn
188 (Galbraith and Kelley, 1996). According to Osborn (1980), the vertical diffusivity (K_z)

189 can be estimated from ε and N by

$$190 \quad K_z = 0.2 \cdot \varepsilon \cdot N^2$$

191 (3)

192 The diffusive nutrient fluxes at the depth of interest can be estimated by multiplying the
193 diffusivity (K_z) by the local nutrient gradient ($\partial C/\partial z$). Nutrient gradient, at the depth of Z_i
194 with the concentration of C_i , is approximately estimated by $(C_{i+1} - C_i)/(Z_{i+1} - Z_i)$, with C_{i+1}
195 the concentrations at Z_{i+1} immediately next to Z_i .

196

197 2.4 Setup of dilution experiments

198 Phytoplankton growth and microzooplankton grazing in the surface waters of stations
199 A and B near the edge of continental shelf were assessed on board using dilution
200 technique (Landry and Hassett, 1982; Landry et al., 1998; Li et al., 2011) on May 13th
201 and May 17th, 2014. All the bottles, tubing and carboys were soaked in 10% (v/v)
202 hydrochloric acid solution for over 24 hours and they were rinsed several times with
203 deionized water and seawater before each experiment. Surface seawater, collected by an
204 acid-washed polyethylene bucket, was screened through a 200- μm mesh before being
205 transferred into polycarbonate carboys as raw seawater. A dilution series was prepared
206 with 0%, 25%, 50%, 75%, and 100% unfiltered seawater in duplicated polycarbonate
207 bottles (0% unfiltered seawater sample was not performed at station B). Measured
208 amounts of particle-free seawater, obtained by filtering the raw seawater with 0.45 μm
209 filters, were added to 2.4-liter polycarbonate bottles. These samples were then enriched
210 with additional nutrients to promote constant growth of phytoplankton. Finally, each
211 bottle was gently filled with unfiltered seawater to its capacity. There was also one bottle
212 filled with 100% unfiltered raw seawater without nutrient enrichment to serve as the
213 control for our experiment. All the bottles were tightly capped and incubated for 24 hours
214 in a deck incubator, which was covered with a neutral density screen to mimic the natural
215 sunlight and filled with flowing seawater from the sea surface to control the temperature.
216 Duplicate 300 ml samples were taken from each bottle before and after the dilution
217 experiments for chlorophyll-*a* measurements.

218 Specific rates of nutrient-saturated phytoplankton growth (μ_n , d^{-1}) and
219 microzooplankton grazing (g , d^{-1}) are estimated by least-square regression between the

220 net growth rates (η , d^{-1}) and the dilution factors (D) as

$$221 \quad \eta = \frac{1}{t} \ln \left(\frac{P_t}{P_0} \right) = \mu_n - D \cdot g \quad (4)$$

223 where P_0 and P_t are the initial and final concentrations of chlorophyll- a , respectively and
224 t is the duration of the incubation. The natural phytoplankton growth rate (μ), which is
225 often subjected to nutrient limitation (Landry et al., 1998), is finally estimated from the
226 net growth rate of raw seawater without nutrient enrichment (η_{raw}) by $\mu = \eta_{\text{raw}} + g$.

227 To examine the response of the phytoplankton community to nutrient enrichment, two
228 bottles of raw seawater with nutrient additions were incubated for 4 days, with
229 chlorophyll- a and nutrient samples taken at the very beginning and each day afterwards.
230 Nutrient data within the exponential growth phase is used to estimate the specific net
231 nutrient consumption rate (m) of the incubated community by linear regression of $\ln(C)$
232 and t assuming

$$233 \quad \frac{dC}{dt} = -m \cdot C \quad (5)$$

234 where C is the concentration of dissolved nutrients in the sample.

236

237 **3. Results**

238 **3.1 Hydrographic dynamics of the nSCS**

239 During the survey of May 2014, waters of the nSCS can be grouped into three regions
240 (Fig. 1): the coastal ocean zone (stations C₁₋₆), the offshore pelagic zone (stations C₇₋₁₀),
241 and the water-intrusion zone near the Luzon Strait (stations C₁₁₋₁₃). These three different
242 zones were influenced by a diverse set of physical processes. The coastal ocean zone,
243 which can be further separated into two subregions including the nearshore area (stations
244 C₁₋₂) and the continental shelf (stations C₃₋₆), was strongly affected by wind-driven
245 upwelling processes including Ekman transport and Ekman pumping (Gan et al., 2010).
246 The nearshore area was characterized by low sea surface temperature (Fig. 2a) as a result
247 of upwelling via Ekman transport driven by southwest monsoon along the shore. Ekman
248 pumping induced by wind stress curl showed a significant increase near the edge of the

249 continental shelf far away from the coastline (Fig. 2b). Upward transport of the deeper
250 water with lower temperature but higher salinity along the shelf slope was clearly seen
251 during the transect (Fig. 3a and 3b), which could be a result of direct upwelling or
252 alongshore advection of upwelled waters from upstream. Both the offshore pelagic zone
253 and the water-intrusion zone are far from the coast with bottom depths more than 2000 m
254 (Fig. 1). The offshore pelagic zone was relatively stable with weak surface geostrophic
255 currents, while the water-intrusion zone was strongly influenced by Kuroshio intrusion
256 through the Luzon Strait (Fig. 2a).

257 Sea surface temperature from satellite showed a generally increasing trend from the
258 coastal regions near Shantou to the offshore regions near Luzon Strait due to the
259 decreasing latitude (Fig. 2a). The observed cross-shelf gradient of surface temperature
260 from the discrete bottle measurements is in good agreement with the satellite SST data,
261 with an average of 24.0 ± 0.6 °C near the coast, 25.2 ± 0.2 °C on the continental shelf,
262 28.4 ± 0.5 °C in the offshore pelagic zone, and 29.1 ± 0.5 °C near the Luzon Strait (Fig.
263 3a). Surface salinity was less variable than temperature from nearshore to offshore with a
264 difference of less than 0.3 during the survey (Fig. 3b). Although there was slightly higher
265 surface salinity on the continental shelf (34.1 ± 0.1), the average salinity concentration at
266 the surface in the coastal ocean zone (33.9 ± 0.2) was generally the same as those of the
267 offshore pelagic zone (33.8 ± 0.1) and the water-intrusion zone (33.9 ± 0.3). Substantially
268 higher subsurface salinities within the euphotic zone between the offshore pelagic zone
269 and the water-intrusion zone (Fig. 3b) could come from the upwelled Pacific waters
270 southwest of Taiwan (Chao et al., 1996).

271 Directions of wind stresses in the nSCS were generally southwest during the study
272 period except two regions where wind stress changed direction (vectors of Fig. 2b): one
273 in the northwest of Dongsha Islands with southerly winds and the other in the Luzon
274 Strait with westerly winds. There were several places of curl-driven upwelling in the
275 offshore deep-water regions, though the entire area was predominantly downwelling.
276 Large curl-driven upwelling ($>0.5 \times 10^{-5}$ m s⁻¹) was only observed near the edge of the
277 continental shelf over abrupt changes of bathymetry. Strong temporal variations of
278 Ekman pumping velocity (Fig. 2d) could be found in the coastal station of C₆ and the
279 offshore station of C₁₃. Though the vertical velocities by Ekman pumping during our

280 sampling duration of May 14th-16th, 2014 are relatively low, they are representative of the
281 entire spring intermonsoon period from May 8th to June 7th, 2014 with substantially low
282 wind intensity (Fig. 2d).

283

284 3.2 Spatial patterns of chlorophyll-*a* and nutrients in the nSCS

285 Sea surface chlorophyll-*a* in the nSCS during May 2014 was very high in the coastal
286 ocean zone – particularly in the near-shore regions – and decreased slightly on the
287 continental shelf (Fig. 2c). In contrast, there was generally low sea surface chlorophyll-*a*
288 in the large areas of the offshore pelagic zone and the water-intrusion zone.

289 Concentrations of the surface chlorophyll-*a* from discrete measurements during our
290 survey (Fig. 3c), varying from 0.04 to 0.92 $\mu\text{g L}^{-1}$, is in good agreement with the satellite
291 remote sensing data. In particular, surface chlorophyll-*a* along the section shows a
292 general seaward-decreasing trend from the costal regions of $0.72 \pm 0.36 \mu\text{g L}^{-1}$ to the
293 offshore regions of $0.09 \pm 0.04 \mu\text{g L}^{-1}$, which is consistent with the decrease of surface
294 nitrate concentrations from $>1.0 \mu\text{mol L}^{-1}$ near coast to $<1.0 \mu\text{mol L}^{-1}$ in offshore (Fig.
295 3d). There was a surface chlorophyll patch ($\sim 0.3 \mu\text{g L}^{-1}$) found at station C₁₁ between the
296 offshore pelagic zone and the water-intrusion zone during the transect study (Fig. 3c),
297 which could result from a surface phytoplankton bloom spreading from the southwest
298 coast of Taiwan to the offshore regions of the central nSCS (Fig. 2c).

299 Phytoplankton chlorophyll-*a* was vertically well mixed in the coastal ocean zone,
300 with clear subsurface maxima of chlorophyll-*a* only found in the offshore pelagic zone
301 and the water-intrusion zone (Fig. 3c). The depth of the subsurface chlorophyll maxima
302 followed the $\sigma_0 = 23.5$ isopycnal, which became much shallower when approaching the
303 continental shelf from offshore. The vertical distribution of nutrients along the section
304 generally followed the isopycnal surfaces in the upper water column (Fig. 3d-f), revealing
305 the importance of physical control on upper ocean biogeochemistry. The observed uplifts
306 of isopycnals as well as the depths of chlorophyll maximum and nutricline at stations C₆,
307 C₈, C₉, C₁₀, and C₁₂ are consistent with positive upwelling velocities driven by wind
308 stress curl (Fig. 2b). Interestingly, there were substantially higher phosphate and silicate
309 concentrations at depths of ~ 200 m (across the $\sigma_0 = 25.5$ isopycnal) for both stations C₉
310 and C₁₁ in the offshore regions, which could be due to either a horizontal or vertical

311 injection event prior to our survey. Elevated chlorophyll-*a* at station C₁₁ was
312 accompanied by not only the subsurface high nutrients but also the high salinity in the
313 euphotic zone, suggesting possible vertical and horizontal nutrient transports in the upper
314 layer. Curiously, low chlorophyll-*a* was found at station C₉, which showed the highest
315 nutrient concentrations and nutrient gradients. Along the density interval of $\sigma_0 = 25$ and σ_0
316 = 26 in the water-intrusion zone there was evidence for isopycnal mixing between the
317 high-nutrient nSCS waters and the adjacent waters of Luzon Strait with lower nutrient but
318 higher temperature/salinity.

319

320 3.3 Vertical diffusivity and diffusive nutrient fluxes

321 Turbulent diffusivity estimated by Thorpe analyses varied substantially from the edge
322 of continental shelf to the west of Luzon Strait during May 2014 (Fig. 4). An overall
323 averaged K_z of $2.5 \times 10^{-4} \text{ m}^2 \text{ s}^{-1}$ for the upper 300 m of the offshore deep-water stations is
324 much higher than the oceanic background diffusivity of $10^{-5} \text{ m}^2 \text{ s}^{-1}$, but is comparable to
325 the previous basin-scale estimates in the nSCS (Tian et al., 2009; Liu and Lozovatsky,
326 2012). There were relatively high mean diffusivities of 3.6×10^{-4} and $3.3 \times 10^{-4} \text{ m}^2 \text{ s}^{-1}$ at
327 stations C₈ and C₁₁, compared to $2.5 \times 10^{-5} \text{ m}^2 \text{ s}^{-1}$ of station C₉. Although the nitrate
328 gradient at the base of euphotic zone in C₉ (0.12 mmol m^{-2}) was about twice of that in
329 C₁₁ (0.06 mmol m^{-2}), its diffusive nitrate flux ($0.26 \text{ mmol m}^{-2} \text{ d}^{-1}$) was only about 15% of
330 that in C₁₁. Our data reveals a general decreasing of mean diffusivity from $1.1 \times 10^{-3} \text{ m}^2 \text{ s}^{-1}$
331 of C₅ on the continental shelf, to $6.3 \times 10^{-4} \text{ m}^2 \text{ s}^{-1}$ of C₆ over the continental slope, and to
332 $9.1 \times 10^{-5} \text{ m}^2 \text{ s}^{-1}$ of C₇ in the offshore pelagic zone. Yang et al. (2014) measured turbulent
333 diffusivity along a short section near the edge of the continental shelf southwest of
334 Taiwan using a microstructure profiler during May 2004 – about the same place as our
335 stations C₅ to C₇ (Fig. 1). Their results showed high turbulent mixing over the continental
336 shelf with a mean diffusivity of $1.6 \times 10^{-3} \text{ m}^2 \text{ s}^{-1}$ but a much lower diffusivity of 5.2×10^{-4}
337 $\text{m}^2 \text{ s}^{-1}$ over the slope (Yang et al., 2014), which are well comparable with our estimates
338 using Thorpe analyses.

339 Due to intermittent nature of the turbulence dissipation, the vertical structures of
340 diffusivity observed during our study were quite patchy (Fig. 4). In order to investigate
341 the vertical patterns of turbulent diffusivity, we compared the observations of the two

342 incubation stations (stations A and B) with that of the reference time-series station S₁ (Fig.
343 5), which had a better vertical resolution of diffusivity. It is not surprising to find that the
344 diffusivity profile of station A is quite similar to that of station S₁ (Fig. 5), as the two
345 stations are very close to each other (Fig. 1). However, there are substantially higher
346 diffusivities found in station B than in station S₁ (Fig. 5). The average diffusivity at 100 m
347 during our study was about $1.6 \times 10^{-4} \text{ m}^2 \text{ s}^{-1}$ in station A but about $4.4 \times 10^{-4} \text{ m}^2 \text{ s}^{-1}$ in station
348 B. The corresponding diffusive nitrate fluxes at the base of euphotic zone were thus about
349 $0.65 \text{ mmol m}^{-2} \text{ d}^{-1}$ in station A and $3.03 \text{ mmol m}^{-2} \text{ d}^{-1}$ in station B, given their nitrate
350 gradients of 0.05 and 0.08 mmol m^{-2} at 100 m, respectively (Table 1). Region of the
351 southeast Dongsha Islands near station B has been well documented for its high turbulent
352 mixing because of internal waves (e.g. Lien et al., 2005; Chow et al., 2008). Enhanced
353 vertical mixing by nonlinear internal waves generated at the shelf edge near Dongsha
354 Islands (Lien et al., 2005) would lead to a higher surface chlorophyll-*a* and net primary
355 production than the adjacent areas with less influence of internal waves during the
356 summertime (Pan et al., 2012). The high diffusivity and diffusive nitrate flux at station B
357 may also be contributed by physical dynamics associated with high internal waves found
358 in this region. The frontal zones at the edge of eddies are often places of increased
359 vertical mixing (Klein and Lapeyre, 2009; Li et al., 2012), though the eddy-induced
360 vertical fluxes may vary substantially between cyclonic, anticyclonic and mode-water
361 eddies (McGillicuddy et al., 2007).

362
363 3.4 Rates of phytoplankton growth, microzooplankton grazing, and specific nutrient
364 consumption

365 Hydrographic and biogeochemical conditions of the two incubation stations were
366 quite different, with much higher temperature (Fig. 6) and salinity (data not shown) but
367 lower nutrients and nutrient gradients in station A than in station B (Fig. 6). Station A was
368 at the edge of a surface phytoplankton bloom (Fig. 2c) spreading from the southwest
369 coast of Taiwan to the offshore pelagic regions, while station B was near the central nSCS
370 with very low sea surface chlorophyll-*a* ($<0.1 \mu\text{g L}^{-1}$). Except for the surface layer,
371 chlorophyll-*a* concentration of station B was generally much higher than that of station A
372 throughout the water column. There was a clear subsurface chlorophyll maximum of ~ 0.4

373 $\mu\text{g L}^{-1}$ at 50 m for station B (Fig. 6), while double peaks of chlorophyll-*a* were found for
374 station A with a surface maximum of $\sim 0.3 \mu\text{g L}^{-1}$ and a subsurface maximum of $\sim 0.1 \mu\text{g}$
375 L^{-1} at 75 m.

376 Rates of phytoplankton growth and microzooplankton grazing at the surface were
377 substantially different between the two stations. The nutrient-saturated phytoplankton
378 growth rate was 1.24 d^{-1} at station B, which was about three times of that at station A
379 (0.44 d^{-1}). On the other hand, the microzooplankton grazing rate of 0.43 d^{-1} at station A
380 was only slightly lower than the grazing rate of 0.60 d^{-1} at station B (Fig. 7). The natural
381 growth rate of phytoplankton, after correction for the effects of nutrient enrichment as
382 described in section 2.3, was 0.28 d^{-1} at station A, much lower than the rate of 1.18 d^{-1} in
383 station B. The rates measured at station B during May 2014 are comparable with previous
384 estimates of growth rates of 1.03 d^{-1} and grazing rates of 0.62 d^{-1} near Dongsha Islands
385 during July 2009 (Chen et al., 2013). Our results for station A are also in good agreement
386 with those found in the non-upwelling area of the south Taiwan Strait (Huang et al., 2011),
387 which suggested mean rates of $0.4\text{--}0.5 \text{ d}^{-1}$ and $0.3\text{--}0.7 \text{ d}^{-1}$ for phytoplankton growth and
388 microzooplankton grazing during July 2004 and 2005.

389 Incubation experiments in station A revealed an exponential growth of phytoplankton
390 chlorophyll-*a* in response to nutrient addition within the first two days, before reaching a
391 stable growth phase on the third day and a decay phase on the fourth day; the
392 chlorophyll-*a* of the control experiment with raw seawater without nutrient additions
393 quickly decreased as nutrients were consumed in the bottles (Fig. 8a). In contrast,
394 phytoplankton of station B showed no response to nutrient enrichment within the first two
395 days of incubation compared to the control experiment (Fig. 8b). Significant increase of
396 incubated chlorophyll-*a* for station B was only found during the last two days of
397 experiment (Fig. 8b). Nutrient utilization during nutrient-enrichment incubations at these
398 two stations were also quite different, with a much slower specific rate of nutrient
399 consumption at station B (0.46 d^{-1}) than at station A (1.03 d^{-1}). These results suggest that
400 there was stronger nutrient limitation of the phytoplankton community at station A than
401 station B during our cruise.

402

403 **4. Discussion**

404 4. 1 Roles of turbulent mixing and curl-driven upwelling on nutrient fluxes of the nSCS
405 during the spring inter-monsoon transition period

406 If the horizontal and atmospheric inputs are ignored, the total nutrient flux into the
407 euphotic zone (J_{total}) is the sum of diffusive flux due to turbulent dissipation ($J_{dif}=K_z \partial C / \partial z$)
408 and the advective flux due to upwelling ($J_{upw}=wC$, negative for downwelling):

$$409 \quad J_{total} = K_z \frac{\partial C}{\partial z} + wC \quad (6)$$

410 To assess the roles of turbulent diffusion and Ekman pumping on vertical transport of
411 nutrients in the nSCS, the diffusive and advective nitrate fluxes at the base of euphotic
412 zone was estimated from the continental shelf to the open sea during May 2014 (see
413 Table 1 for details). Vertical velocity (w) at the base of euphotic zone is assumed equal
414 to the curl-driven upwelling/downwelling velocity (w_e) by Ekman pumping. We have
415 neglected Ekman transport as its effect is restricted only to the near coast (Gan et al.,
416 2010). Variations of w during the transect study is consistent with the isopycnal
417 oscillation along the section (Fig. 3), suggesting the important role of Ekman pumping on
418 physical dynamics of the water column. At the continental slope of station C₆, the vertical
419 nitrate fluxes were largely supported by curl-driven upwelling, with turbulent mixing
420 playing a minor role due to low nitrate gradients. In contrast, the diffusive nitrate flux
421 was over three times of the upwelled nitrate flux at station C₇, immediately adjacent to C₆.
422 Except for station C₁₂, curl-driven downwelling was observed in the deep-water regions
423 during the transect study, leading to downward transport of the low-nutrient surface water
424 to the deeper layer. The upward nitrate fluxes in these stations were thus determined by
425 the intensities of diffusive fluxes working against the downwelling fluxes. There was a
426 negative nitrate flux found at station C₉ where downwelling was stronger than the upward
427 diffusion, resulting in a loss of nitrate from the euphotic zone. Our findings suggest that it
428 is the interplay of turbulent diffusion and curl-driven upwelling/downwelling that
429 controls the vertical fluxes of nutrients into the euphotic zone to support phytoplankton
430 production in the nSCS.

432 For the deep-water stations including the offshore pelagic zone and the water
433 intrusion zone, the integrated chlorophyll-*a* biomass during the transect study shows a

positive correlation with the upward nitrate flux ($\int Chl \cdot dz = 16.75 \times J_{total} + 7.7$, $r^2 = 0.58$, $p = 0.014$) when stations C₉ is not included (Table 1), supporting the important role of bottom-up control on phytoplankton production in our study area (Chen, 2005). Station C₆ should be excluded from the regression since it is near the top of the shelf-slope subjecting to influence by along-shelf transport of low-chlorophyll waters, which could have resulted in the relatively lower chlorophyll-*a* biomass but higher vertical nutrient supplies observed in this station. From the regression slope of 16.75, we could estimate a specific new production by vertical nitrate supply of 0.060 molN (gChl)⁻¹ d⁻¹, which is slightly lower than 0.063-0.088 molN (gChl)⁻¹ d⁻¹ reported in the nSCS by Chen (2005). Assuming a vertically constant rate of phytoplankton specific growth, a gram chlorophyll-to-carbon ratio of 0.03 and a molar C/N ratio of 6.625, we estimate a vertically integrated primary production of ~ 12.3 mmolN m⁻² d⁻¹ in station B and ~ 1.8 mmolN m⁻² d⁻¹ in station A. The contribution of vertical nutrient fluxes to primary production could thus be $\sim 11\%$ and $\sim 26\%$ in stations B and A, respectively, which are comparable with the *f*-ratio of 0.14-0.20 previously estimated in the nSCS from late March to October (Chen, 2005). In steady status, the net primary production of phytoplankton should be balanced by the upward nutrient flux as well as the downward particle flux. Therefore, a high nutrient flux would correspond to a high net primary production and thus a high biomass accumulation, if other conditions remain the same (species, temperature, light, grazing, etc). Station C₉ is interesting in that the vertical nutrient fluxes are net downward out of the euphotic zone, suggesting that the station may not be in steady status. High nutrients here are likely a result of strong horizontal input or a previous diapycnal nutrient injection. In this case, large drawdown of nutrients may be expected by fast growing phytoplankton and by the downward transport of nutrients out of euphotic zone.

Uncertainty of the vertical nutrient flux could be contributed by errors in the determinations of vertical diffusivity and vertical velocity, as well as nutrient concentration and gradient. Calculation errors of vertical diffusivity by the Thorpe-scale approach, estimated from the time-series station S₁, were 0.87×10^{-4} m⁻² s⁻¹ at 50 m ($n=5$), 0.71×10^{-4} m⁻² s⁻¹ at 100 m ($n=6$), and 0.46×10^{-4} m⁻² s⁻¹ at 150 m ($n=7$). We therefore obtain an average of 0.68×10^{-4} m⁻² s⁻¹ for the overall uncertainty of diffusivity

465 determined in our study. Uncertainty of vertical velocity by Ekman pumping from
466 satellite observations could be approximately determined at each station by their standard
467 deviations over the sampling duration of May 14th-16th, 2014. Measurement errors of
468 nutrients at depths during the field study should be negligible as the concentrations are
469 considerably higher than the detection limits of the analytical methods. We are not able to
470 quantify the uncertainty of nutrient gradient, as we have only one cast for each station
471 with reduced resolution below the euphotic layer. Meanwhile, the nutrient gradient and
472 related diffusive flux that we have calculated at the base of euphotic zone could be
473 interpreted as a mean value between the two adjacent bottle depths (100-200 m). The
474 final uncertainties for the vertical nutrient fluxes are summarized in Table 1, which vary
475 substantially from 0.34 to 0.98 mmol m⁻² d⁻¹ ($n=9$) for stations in the offshore regions.

476

477 4.2 Impact of growth-grazing dynamics on phytoplankton chlorophyll biomass in the
478 nSCS

479 Distributions of phytoplankton in the ocean are controlled by complex physical and
480 biological interactions. To assess the influence of growth-grazing dynamics on
481 phytoplankton chlorophyll-*a* biomass in the nSCS, two stations with distinct
482 biogeochemical settings and nutrient fluxes were selected for measurements of
483 phytoplankton growth and microzooplankton grazing rates. In addition, the community
484 response to nutrient enrichments at the two stations was assessed by continuous
485 incubations for up to four days. Previous studies indicates that surface phytoplankton
486 community in the southeast Dongsha Islands is dominated by both diatom and
487 picoplankton such as *Prochlorococcus*, while picoplankton with negligible diatoms are
488 found in the non-upwelling area south of the Taiwan Strait during late spring and early
489 summer (Yang, 2009; Huang et al., 2011). Our results of substantially high phytoplankton
490 growth rates observed at station B southeast of Dongsha Islands are in agreement with its
491 high nutrient concentrations and nutrient fluxes compared to station A south of Taiwan
492 Strait. When released from the constraints by nutrient limitation, phytoplankton
493 community will be expected to shift from dominance by picoplankton toward a higher
494 relative abundance of larger phytoplankton because of their higher intrinsic capacity for
495 growth (Agawin et al., 2000).

496 Percentage of the primary production consumed by microzooplankton can be
497 estimated by the ratio of microzooplankton grazing over phytoplankton growth (g/μ)
498 (Landry et al., 1998). High g/μ ratios (~ 1.5) at station A suggest an elevated role of the
499 microbial food web in the south Taiwan Strait, promoting nutrient recycling to support
500 further phytoplankton growth. Whereas, the relatively higher microzooplankton grazing
501 rate but lower g/μ ratio at station B may indicate a greater efficiency of carbon export
502 near the Dongsha Islands, as the greater loss of diatoms through sinking or grazing by
503 mesozooplankton in regions with high nutrient supply (Landry et al., 1998). Natural
504 growth of phytoplankton at station B was much higher than its grazing mortality, leading
505 to a large net growth rate (growth minus grazing) of 0.58 d^{-1} , which is consistent with the
506 high integrated chlorophyll biomass in this station. In contrast, a negative net growth rate
507 of -0.15 d^{-1} was found at station A as a result of higher grazing pressure. The specific
508 phosphate consumption rate of 1.03 d^{-1} at station A was about twice of that at station B
509 (0.46 d^{-1}) suggesting a larger nutrient demand at station A. There was actually a faster
510 response of phytoplankton to nutrient enrichment at station A than at station B indicating
511 a stronger nutrient limitation in the south Taiwan Strait. The negative net community
512 growth and the higher nutrient consumption rate at station A are consistent with the
513 spring phytoplankton bloom of the southwest Taiwan observed in the satellite data (Fig.
514 2c) being in its decline phase. Indeed, the area of the phytoplankton bloom decreased
515 substantially within two weeks and was not visible by the middle of June, 2014 (from
516 weekly mean sea surface chlorophyll-*a* data of MODIS Aqua) supporting the important
517 role of grazing activity on phytoplankton distribution in the nSCS.

518 In conclusion, we have conducted a preliminary study on vertical nutrient fluxes and
519 phytoplankton dynamics in the nSCS. Our results suggest that phytoplankton patchiness
520 in the nSCS during the spring inter-monsoon of May 2014 was largely controlled by
521 vertical nutrient fluxes, which were driven by both turbulent diffusion and wind stress
522 curl-driven upwelling. Our results also revealed an increasing role of turbulent diffusion
523 but a decreasing role of curl-driven upwelling in vertical transport of nutrients from the
524 coastal ocean zones to the offshore pelagic zones in the nSCS. Elevated nutrient fluxes
525 observed near the Dongsha Islands were found to support high new production leading to
526 net growth of phytoplankton community, whereas the low nutrient fluxes of the south

527 Taiwan Strait resulted in a negative net community growth leading to decline of a
528 phytoplankton bloom. As the findings presented here is limited by the very narrow area
529 and the very short period of sampling time, future studies may be improved by addressing
530 the variability of vertical nutrient fluxes and its relationship to phytoplankton dynamics
531 on a much longer time scale over a much broader area of the nSCS.

532

533 *Acknowledgements*

534 We are grateful to the captain and crew of the *R/V Shiyuan III* for their helps during the
535 field work. We also thank two anonymous reviewers for helpful comments. This work is
536 supported by a startup fund from a National Talent-Recruitment Program and a grant
537 from the Chinese Academy of Sciences' Strategic Pilot Project No.XDA110202014 (to
538 QPL).

539 *References*

540 Abraham, E.R.: The generation of plankton patchiness by turbulent stirring, *Nature*, 391,
541 577-580, 1998.

542 Agawin, N.S.R., Duarte, C.M., and Agusti, S.: Nutrient and temperature control of the
543 contribution of picoplankton to phytoplankton biomass and production, *Limnol. Oceanogr.*, 45,
544 591-600, 2000.

545 Bombar, D., Dippner, J.W., Doan, H.N., Ngoc, L.N., Liskow, I., Loick-Wilde, N., and Voss,
546 M.: Sources of new nitrogen in the Vietnamese upwelling region of the South China Sea, *J.*
547 *Geophys. Res.*, 115, C06018, doi:10.1029/2008JC005154, 2010.

548 Centurioni, L.R., Niiler, P.P., and Lee, D.K.: Observations of inflow of Philippine Sea surface
549 water into the South China Sea through the Luzon Strait, *J. Phys. Oceanogr.*, 34, 113-121, 2004.

550 Chao, S.Y., Shaw, P.T., and Wu, S.Y.: Deep water ventilation in the South China Sea,
551 *Deep-Sea Res.*, I 43, 445-466, 1996.

552 Chen, B., Liu, H., Landry, M.R., Dai, M., Huang, B., and Sun, J.: Close coupling between
553 phytoplankton growth and microzooplankton grazing in the western South China Sea, *Limnol.*
554 *Oceanogr.*, 54, 1084-1097, 2009.

555 Chen, B., Zheng, L., Huang, B., Song, S., and Liu, H.: Seasonal and spatial comparisons of
556 phytoplankton growth and mortality rates due to microzooplankton grazing in the northern South
557 China Sea, *Biogeosciences*, 10, 2775-2785, 2013.

558 Chen, Y.L.: Spatial and seasonal variations of nitrate-based new production and primary
559 production in the South China Sea, *Deep-Sea Res.*, II, 52, 319-340, 2005

560 Chow, C., Hu, J., Centurioni, L.R., and Niiler, P.P.: Mesoscale Dongsha cyclonic eddy in the
561 northern South China Sea by drifter and satellite observations, *J. Geophys. Res.*, 113, C04018,
562 doi:10.1029/2007JC004542, 2008.

563 Cullen, J.J., Franks, P.J.S., Karl, D.M., and Longhurst, A.: Physical influences on marine
564 ecosystem dynamics, in: *The sea*, 12, Robinson, A.R., McCarthy, J.J., Rothschild, B.J. (eds), John
565 Wiley & Sons, New York, 297-336, 2002.

566 Davis, C.S., Flierl, G.R., Wiebe, P.H., and Franks, P.J.S.: Micropatchiness, turbulence and
567 recruitment in plankton, *J. Mar. Res.*, 43, 109-151, 1991.

568 Eppley, R.W., and Peterson, B.J.: Particulate organic matter flux and planktonic new
569 production in the deep ocean, *Nature*, 282, 677-680, 1979.

570 Farris, A., and Wimbush, M.: Wind-induced intrusion into the South China Sea, *J. Oceanogr.*,
571 52, 771-784, 1996.

572 Galbraith, P.S., and Kelley, D.E.: Identifying Overturns in CTD Profiles, *J. Atmos. Ocean.*

573 Tech., 13, 688–702, 1996.

574 Gan, J., Lu, Z., Dai, M., Cheung, A., Liu, H., and Harrison, P.: Biological response to
575 intensified upwelling and to a river plume in the northeastern South China Sea: A modeling study,
576 J. Geophys. Res., 115, doi: 10.1029/2009jc005569, 2010.

577 Gargett, A. E., and Garner, T.: Determining Thorpe scales from ship-lowered CTD density
578 profiles, J. Atmos. Ocean. Tech., 25, 1657–1670, 2008.

579 Gaube, P., Chelton, D.B., Strutton, P.G., and Behrenfeld, M.J.: Satellite observations of
580 chlorophyll, phytoplankton biomass, and Ekman pumping in nonlinear mesoscale eddies, J.
581 Geophys. Res., 118, 6349-6370, doi:10.1002/2013JC009027, 2013.

582 Gill, A.E. (Eds.): *Atmosphere-Ocean Dynamics*, International Geophysics Series, 30,
583 Academic Press, London, 1982.

584 Han, A., Dai, M., Gan, J., Kao, S., Zhao, X., Jan, S., Li, Q., Lin, H., Chen, C., Wang, L., Hu,
585 J. Wang, L., and Gong, F.: Inter-shelf nutrient transport from the East China Sea as a major
586 nutrient source supporting winter primary production on the northeaster South China Sea shelf,
587 Biogeosciences, 10, 8159-8170, 2013.

588 Huang, B., Xiang, W., Zeng, X., Chiang, K., Tian, H., Hu, J., Lan, W., and Hong, H.:
589 Phytoplankton growth and microzooplankton grazing in a subtropical coastal upwelling system in
590 the Taiwan Strait, Cont. Shelf Res., 31, 48-56, 2011.

591 Kim, T.K., Lee, K., Duce, R., Liss, P.: Impact of atmospheric nitrogen deposition on
592 phytoplankton productivity in the South China Sea, Geophys. Res. Letters, 41(9), 3156-3162,
593 2013.

594 Klein, P., and Lapeyre, G.: The oceanic vertical pump induced by mesoscale and
595 submesoscale turbulence, Annu. Rev. Mar. Sci., 1, 351-375, 2009.

596 Landry, M.R., Brown, S.L., Campbell, L., Constantinou, J., and Liu, B.: Spatial patterns in
597 phytoplankton growth and microzooplankton grazing in the Arabian Sea during monsoon forcing,
598 Deep-Sea Res., II, 45, 2353-2368, 1998.

599 Landry, M.R., and Hassett, R. P.: Estimating the grazing impact of marine micro-zooplankton,
600 Mar. Biol., 67(3), 283-288, 1982.

601 Li, Q.P., Franks, P.J.S., and Landry, M.R.: Microzooplankton grazing dynamics:
602 parameterizing grazing models with dilution experiment data in the California Current Ecosystem,
603 Mar. Ecol. Prog. Ser., 438, 59-69, 2011.

604 Li, Q.P., Franks, P.J.S., Ohman, M.D., and Landry, M.R.: Enhanced nitrate flux and biological
605 processes in a frontal zone of the California Current System, J. Plankton Res., 34, 790-801, 2012.

606 Li, Q.P., and Hansell, D.A.: Nutrient distribution in baroclinic eddies of the oligotrophic

607 North Atlantic and inferred impacts on biology, *Deep-Sea Res.*, II, 55, 1291-1299, 2008.

608 Li, Q.P., Hansell, D.A., and Zhang, J.Z.: Underway monitoring of nanomolar nitrate plus
609 nitrite and phosphate in oligotrophic seawater, *Limnol. Oceanogr. Methods*, 6, 319-326, 2008.

610 Li, Q.P., Wang, Y., Dong, Y., and Gan, J.: Modeling long-term change of planktonic
611 ecosystems in the Northern South China Sea and the upstream Kuroshio Current, *J. Geophys.*
612 *Res.*, 120, doi:10.1002/2014JC010609, 2015

613 Lien, R., Tang, T., Chang, M., and D'Asaro, E.A.: Energy of nonlinear internal waves in the
614 South China Sea, *Geophys. Res. Lett.*, 32, L05615, doi:10.1029/2004GL022012, 2005.

615 Lin, I., Lien, C., Wu, C., Wong, G.T.F., Huang, C., and Chiang, T.: Enhanced primary
616 production in the oligotrophic South China Sea by eddy injection in spring, *Geophys. Res. Letters*,
617 37, L16602, doi:10.1029/2010GL043872, 2010.

618 Lin, I., Wong, G.T.F., Lien, C., Chien, C., Huang, C., and Chen, J.: Aerosol impact on the
619 South China Sea biogeochemistry: an early assessment from remote sensing, *Geophys. Res.*
620 *Letters*, 36, L17605, doi:10.1029/2009GL037484, 2009.

621 Liu, K.K., Chao, S.Y., Shaw, P.T., Gong, G.C., Chen, C.C., and Tang, T.Y.: Monsoon-forced
622 chlorophyll distribution and primary production in the South China Sea: observations and a
623 numerical study, *Deep-Sea Res.*, I, 49, 1387-1412, 2002.

624 Liu, X., Furuya, K., Shiozaki, T., Masuda, T., Kodama, T., Sato, M., Kaneko, H., Nagasawa,
625 M., and Yasuda, I.: Variability in nitrogen sources for new production in the vicinity of the shelf
626 edge of the East China Sea in summer, *Cont., Shelf Res.*, 61-62, 23-30, 2013.

627 Liu, Z.Y., and Lozovatsky, I.: Upper pycnocline turbulence in the northern South China Sea,
628 *Chin. Sci. Bull.*, 57(18), 2302-2306, 2012.

629 McGillicuddy, D.J., Anderson, L., Bates, N., Bibby, T., Buesseler, K., Carlson, C., Davis, C.,
630 Ewart, C., Falkowski, P., Goldthwait, S., Hansell, D.A., Jenkins, W.J., Johnson, R., Kosnyrev, V.,
631 Ledwell, J.R., Li, Q.P., Siegel, D.A., and Steinberg, D.K.: Eddy-wind interactions stimulate
632 extraordinary mid-ocean plankton blooms, *Science*, 316, 1021-1026, 2007.

633 Osborn, T.R.: Estimates of the local rate of vertical diffusion from dissipation measurements,
634 *J. Phys. Oceanogr.*, 10(1), 83-89, 1980.

635 Pan, X., Wong, G.T.F., Shiah, F.K., and Ho, T.Y.: Enhancement of biological production by
636 internal waves: observations in the summertime in the northern South China Sea, *J. Oceanogr.*, 68,
637 427-437, 2012.

638 Parsons, T.R., Maita, Y., and Lalli, C.M. (Eds.): *A manual of chemical and biological methods*
639 for seawater analysis, Pergamum Press, Oxford, 1984.

640 Risien, C.M., and Chelton, D.B.: A global climatology of surface wind and wind stress fields

641 from eight year QuickSCAT scatterometer data, *J. Phys. Oceanogr.*, 38, 2379-2412, 2008.

642 Rykaczewski, R.R., and Checkley, D.M.: Influence of ocean winds on the pelagic ecosystem
643 in upwelling regions, *PNAS*, 105(6), 1065–1970, 2008.

644 Strom, S. L., Macri, E. L., and Olson, M. B.: Microzooplankton grazing in the coastal Gulf of
645 Alaska: Variations in top-down control of phytoplankton, *Limnol. Oceanogr.*, 52, 1480–1494,
646 2007.

647 Tian, J., Yang, Q., and Zhao, W.: Enhanced diapycnal mixing in the South China Sea. *J. Phys.*
648 *Oceanogr.*, 39, 3191-3203, 2009.

649 Thorpe, S.A.: Turbulence and mixing in a Scottish loch, *Phil. Trans. Royal Soc., London A*,
650 286, 125–181, 1977.

651 Wang, J., and Tang, D.: Phytoplankton patchiness during spring intermonsoon in west coast
652 of South China Sea, *Deep-Sea Res, II*, 101, 120-128, 2014.

653 Yang, Q., Tian, J., Zhao, W., Liang, X., and Zhou, L.: Observations of turbulence on the shelf
654 and slope of northern South China Sea, *Deep-Sea Res., I*, 87, 43-52, 2014.

655 Yang, Y.H.: Phytoplankton community structure of the northern South China Sea and the
656 Philippine Sea, Master Thesis (in CHN), National Taiwan Normal University, Taiwan, 73 pp.,
657 2009.

658 Zhou, L., Tan, Y., Huang, L., Huang, J., Liu, H., and Lian, X.: Phytoplankton growth and
659 microzooplankton grazing in the continental shelf area of northeastern South China Sea after
660 typhoon Fengshen, *Cont. Shelf Res.*, 31, 1663-1671, 2011.

661 Table 1: Comparisons of integrated chlorophyll-*a* ($\int Chl \cdot dz$), nitrate gradient ($\partial C/\partial z$), nitrate
662 concentration (NO_3), vertical diffusivity (K_z), upwelling velocity (w_e), diffusive nitrate flux
663 (J_{dif}), upwelled nitrate flux (J_{upw}), and total nitrate flux (J_{total}) for transect stations C₆₋₁₂ and
664 incubation stations A and B at ~1% light depth (~100m depth).

Station	$\int Chl \cdot dz$ [mg m ⁻²]	$\partial C/\partial z$ [mmol m ⁻⁴]	NO_3 [mmol m ⁻³]	^a K_z [10^{-4} m ² s ⁻¹]	^b w_e [10^{-5} m s ⁻¹]	J_{dif} [mmol m ⁻² d ⁻¹]	^c J_{upw} [mmol m ⁻² d ⁻¹]	J_{total} [mmol m ⁻² d ⁻¹]
C ₆	16.8	0.001	5.01	6.30±0.68	0.28±0.02	0.05±0.01	1.21±0.09	1.27±0.10
C ₇	20.2	0.077	6.42	0.91±0.68	0.03±0.05	0.60±0.45	0.17±0.27	0.77±0.73
C ₈	22.1	0.079	7.47	3.60±0.68	-0.21±0.08	2.44±0.46	-1.36±0.52	1.09±0.98
C ₉	15.4	0.122	9.52	0.25±0.68	-0.12±0.03	0.26±0.72	-0.99±0.25	-0.72±0.96
C ₁₀	21.7	0.082	9.37	3.45±0.68	-0.18±0.03	2.44±0.48	-1.46±0.24	0.99±0.72
C ₁₁	38.7	0.060	2.08	3.30±0.68	-0.27±0.07	1.71±0.35	-0.49±0.13	1.23±0.48
C ₁₂	20.7	0.029	3.93	1.53±0.68	0.05±0.05	0.39±0.17	0.17±0.17	0.56±0.34
C ₁₃	13.2	0.046	1.98	2.26±0.68	-0.27±0.17	0.91±0.27	-0.46±0.29	0.44±0.56
A	15.7	0.047	2.09	1.60±0.68	-0.09±0.04	0.65±0.28	-0.16±0.08	0.49±0.35
B	24.8	0.080	4.82	4.40±0.68	-0.41±0.11	3.03±0.47	-1.71±0.46	1.33±0.93

665

666 ^a uncertainty of K_z from Thorpe analyses is estimated as 0.68×10^{-4} m² s⁻¹ (see text for detail)

667 ^b w_e are 3-day-mean of May 14th-16th, 2014, except station B that is of May 12th-14th, 2014

668 ^c assuming vertical velocity at the depth of 100m is equal to w_e .

669 Figure 1: Sampling map in the northeastern South China Sea during May 2014. Dash
 670 lines show the topography of the study area; solid dots are the stations for a transect study
 671 (C₁₋₁₃) during May 14th-16th, 2014; star is a time-series reference station (S₁); filled
 672 squares are two stations where shipboard dilution experiments were performed (A and B).
 673 Inserted plot shows the temperature/salinity diagram for the transect with arrows
 674 indicating waters from the coastal ocean zone (thick gray lines), the offshore pelagic zone
 675 (thick black lines), and the Kuroshio intrusion zone (thin lines).

676

677 Figure 2: Spatial distributions of (a) sea surface temperature, (b) curl-driven upwelling
 678 velocity, and (c) sea surface chlorophyll during the survey, together with (d) the
 679 time-series of curl-driven upwelling and wind stress at stations C₆ and C₁₃ during
 680 May-June, 2014. Vectors in panel (a) and panel (b) are surface geostrophic currents and
 681 wind stresses, respectively; geostrophic current is from OSCAR data; upwelling velocity
 682 and wind stress are from 3-day mean METOP-ASCAT data; sea surface temperature is
 683 3-day-mean GOES-POES data; sea surface chlorophyll-*a* is monthly MODIS-Aqua data.

684

685 Figure 3: Vertical distributions of (a) temperature [T], (b) salinity [S], (c) chlorophyll-*a*
 686 [Chl-*a*], (d) nitrate [NO₃], (e) silicate [Si(OH)₄], and (f) phosphate [PO₄] along the coastal
 687 transect of the northern South China Sea. Overlaid white lines in each panel are
 688 isopycnals.

689

690 Figure 4: Profiles of Thorpe displacement (d_z), Thorpe scale (L_T), and turbulent
 691 diffusivity (K_z) for nine stations (C₅, C₆, C₇, C₈, C₉, C₁₀, C₁₁, C₁₂, C₁₃) from the edge of
 692 continental shelf to the west of Luzon Strait. Locations of these stations are shown in
 693 Figure 1.

694

695 Figure 5: Comparisons of vertical turbulent diffusivities (K_z) between two stations A and
 696 B. Black line is the result of the reference station S₁ with continuous CTD sampling up to
 697 13 casts; circles are for station A (2 casts) with squares for station B (2 casts).

698

699 Figure 6: Comparisons of vertical profiles of chlorophyll-*a* [Chl-*a*], temperature [T],
 700 nutrients [Si(OH)₄, NO₃, PO₄], and nutrient gradients between two incubation stations A
 701 and B. Thick lines in each panel are for bottom axis with thin lines (open symbols) for top
 702 axis; dash lines are for station A with solid lines for station B.

703

704 Figure 7: Dilution experiment plots of phytoplankton net growth rates against the dilution
 705 factors for stations A and B. Filled circles are net growth rates of the raw seawater
 706 without nutrient enrichments.

707

708 Figure 8: Temporal variations of chlorophyll-*a* [Chl-*a*] and phosphate [PO₄] during
 709 incubations with and without nutrient enrichments in stations A and B. Dash lines (filled
 710 symbols) are for chlorophyll-*a* in left axis with thin lines (open symbols) for phosphate in
 711 right axis; control is the incubation of raw seawater without nutrient addition.

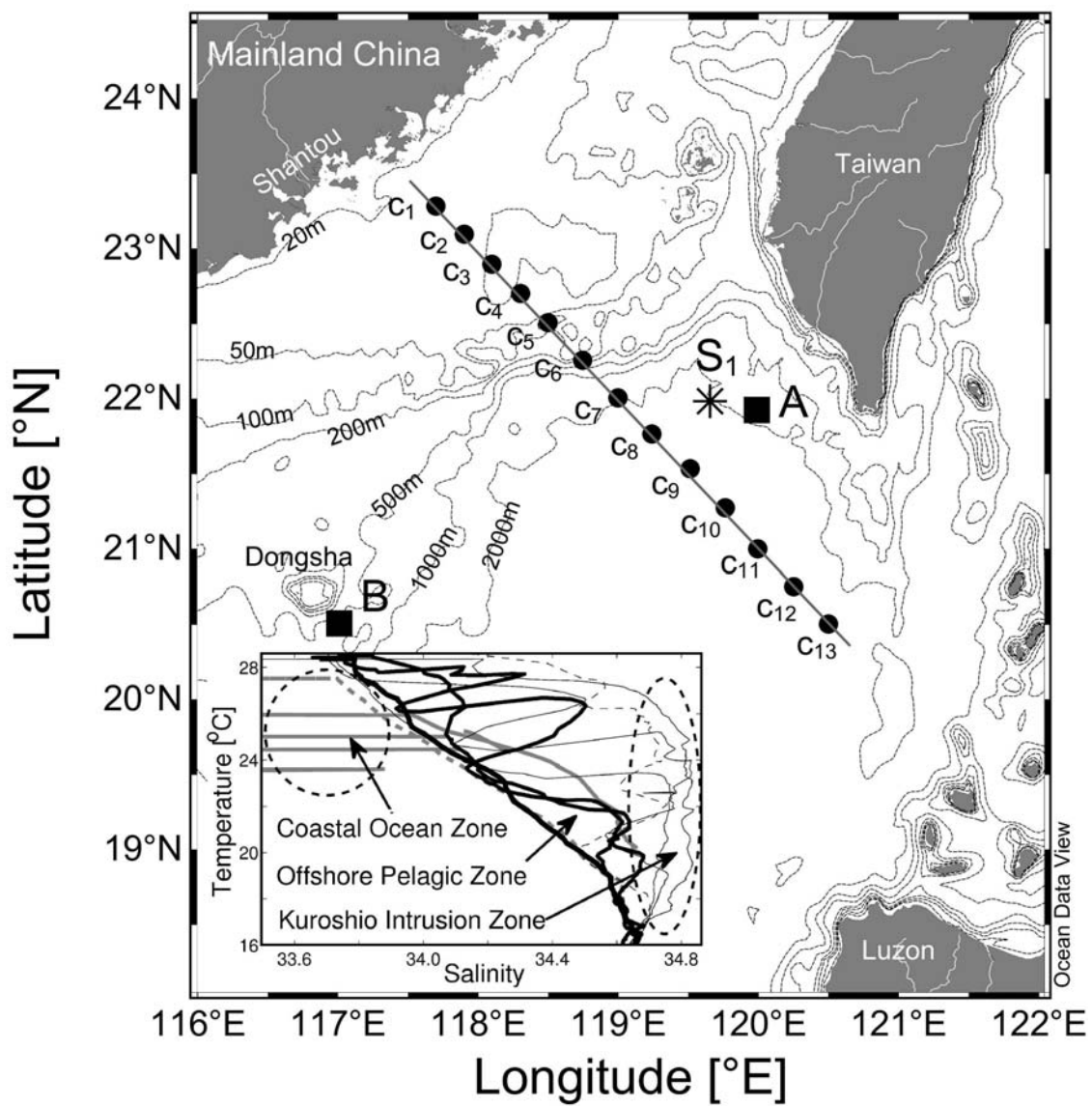


Figure 1

712
713
714

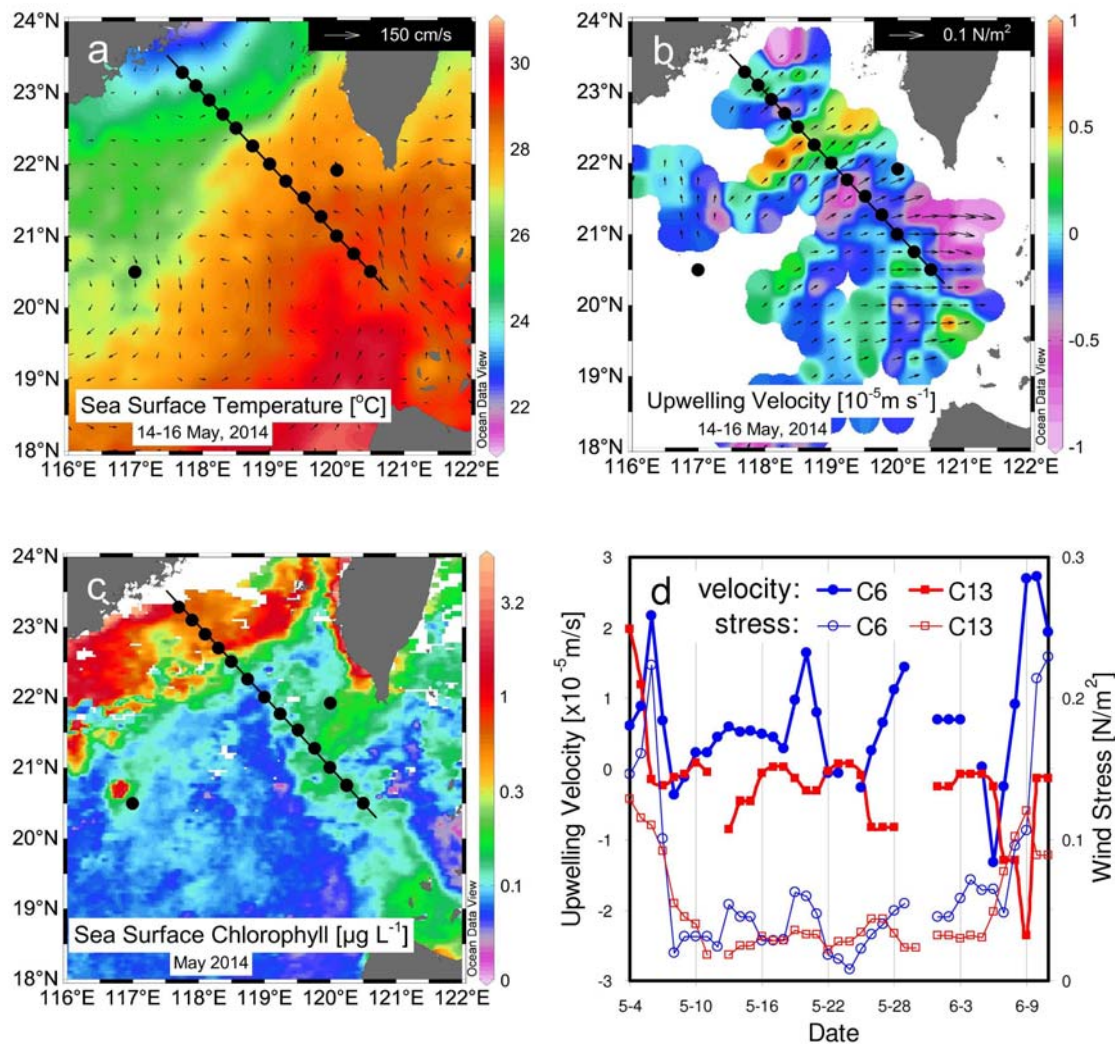


Figure 2

718

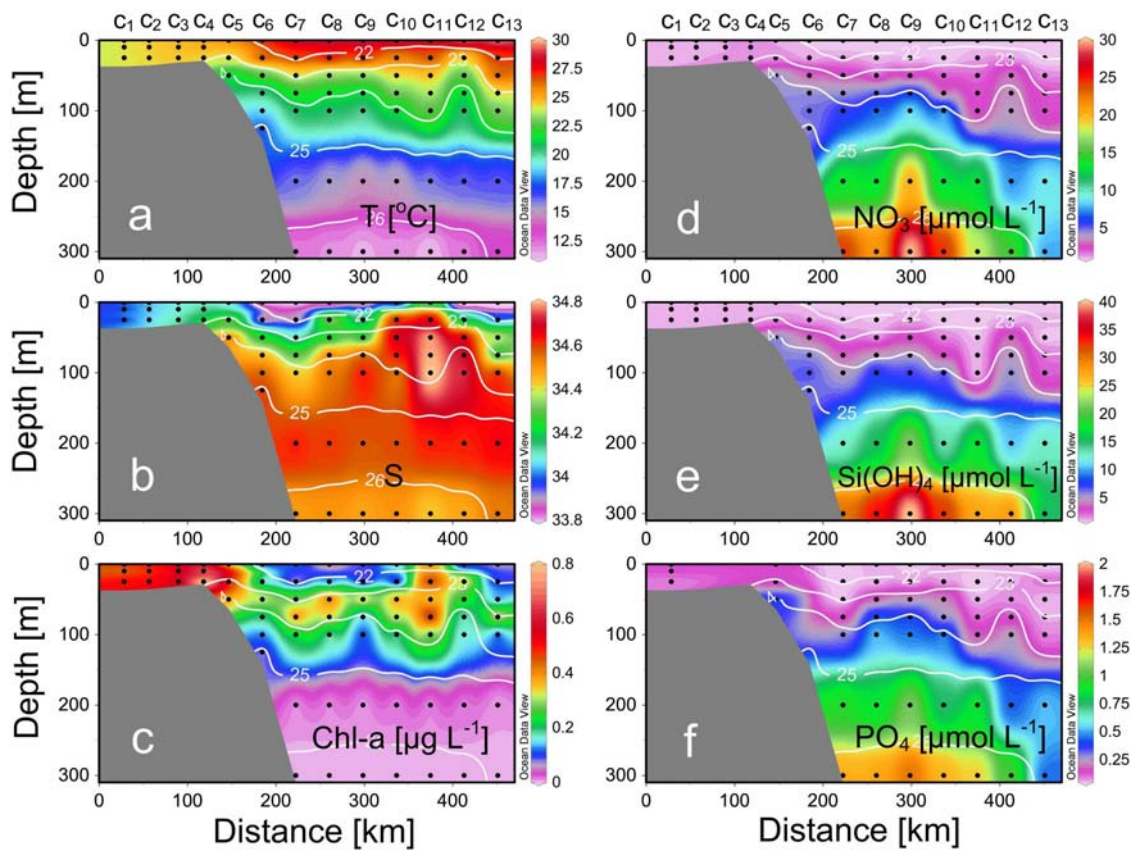
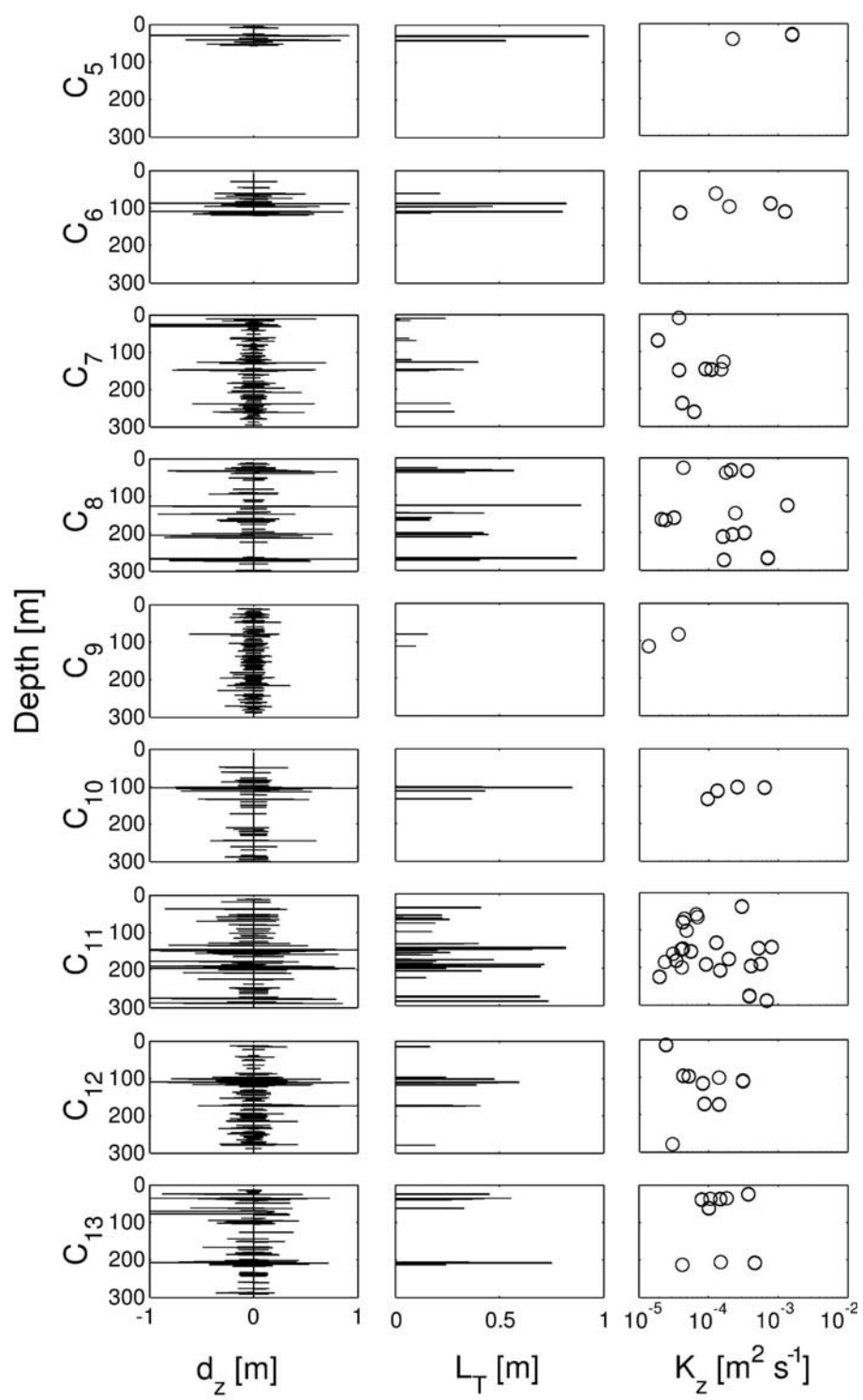


Figure 3

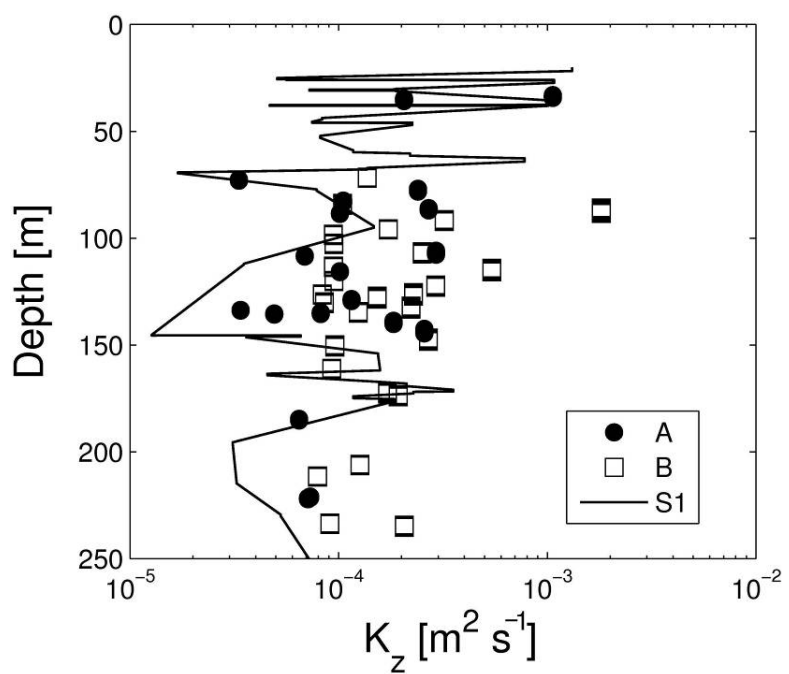
719

720



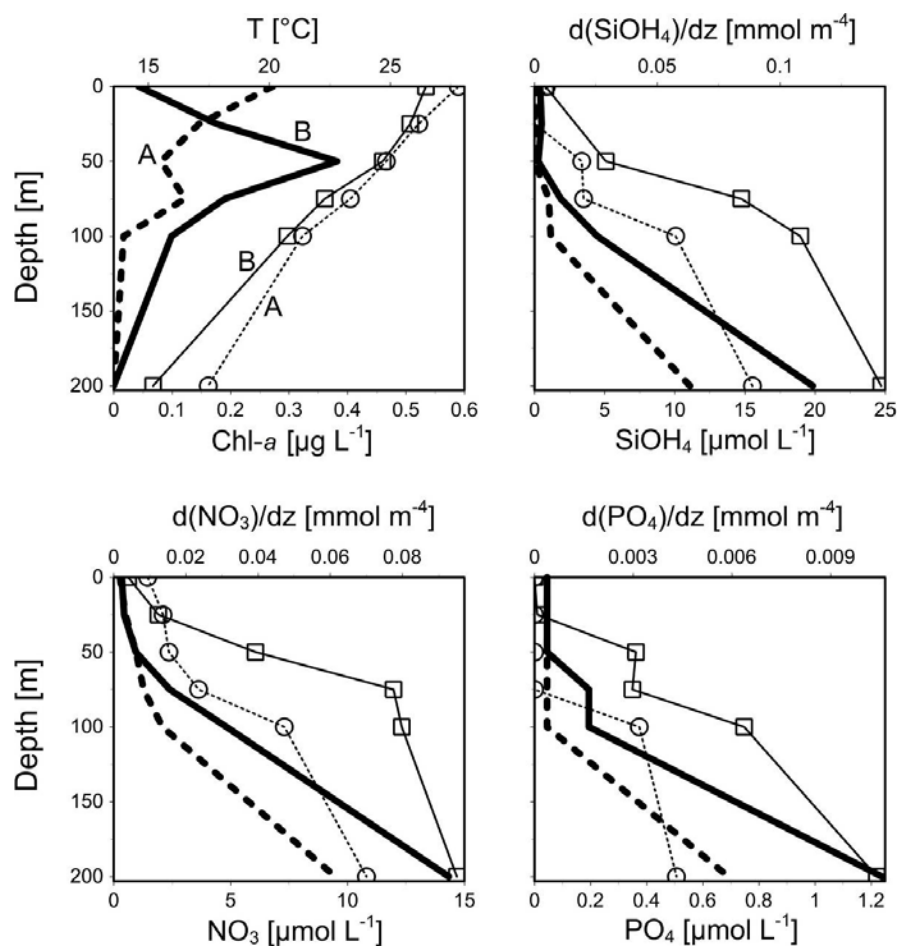
721
722
723

Figure 4



724
725
726

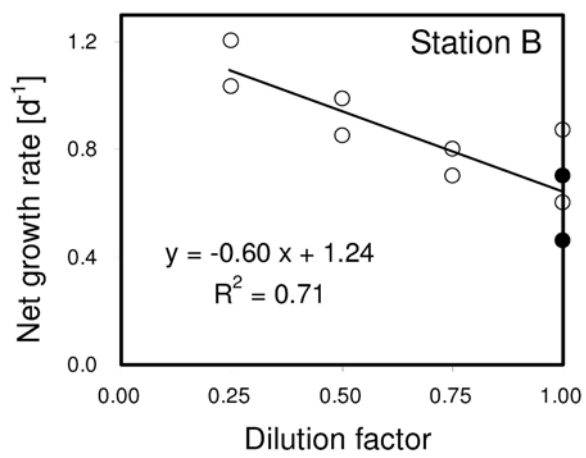
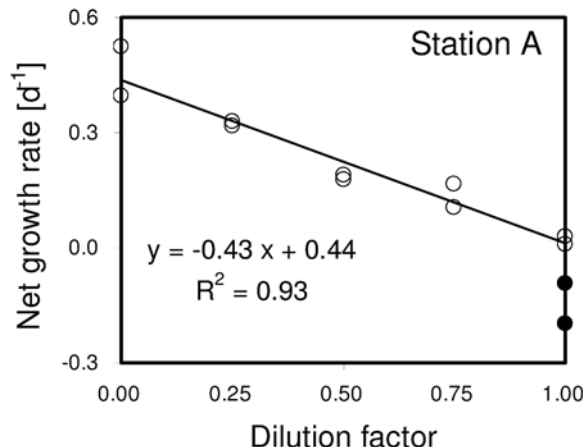
Figure 5



727
728
729

Figure 6

730



731

732

733

734

Figure 7

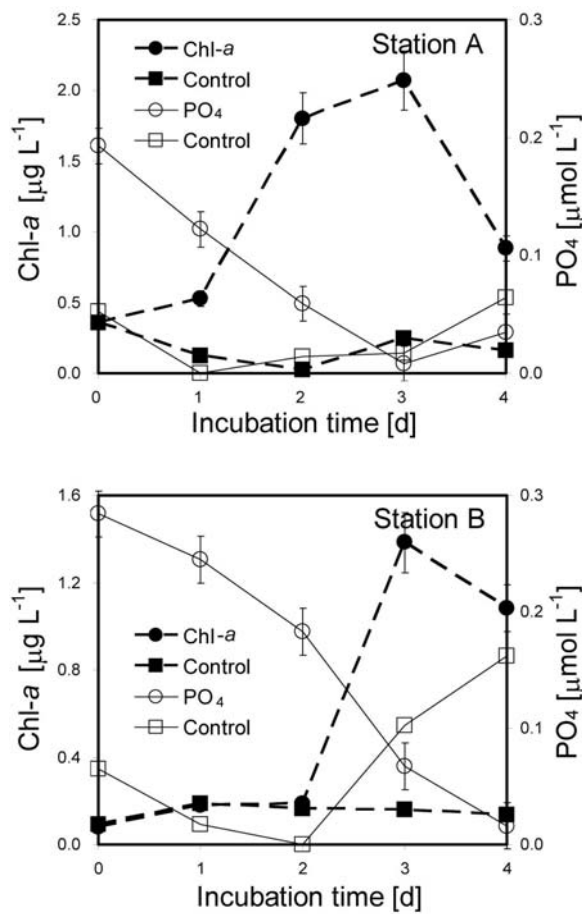


Figure 8